



Article

# Synthesis of Si, N co-Doped Nano-Sized TiO<sub>2</sub> with High Thermal Stability and Photocatalytic Activity by Mechanochemical Method

Peisan Wang<sup>1,2</sup> , Chunxia Qi<sup>3</sup>, Pengchao Wen<sup>1</sup>, Luyuan Hao<sup>1</sup>, Xin Xu<sup>1,\*</sup> and Simeon Agathopoulos<sup>4</sup>

<sup>1</sup> Chinese Academy of Science, Key Laboratory of Materials for Energy Conversion, Department of Materials Science and Engineering, University of Science and Technology of China, Hefei 230032, China; wpsan@mail.ustc.edu.cn (P.W.); wpc39@mail.ustc.edu.cn (P.W.); hly@ustc.edu.cn (L.H.)

<sup>2</sup> Department of Chemistry, Anhui Medical University, Hefei 230032, China

<sup>3</sup> Department of Chemical Engineering, Hefei Normal University, Hefei Lianhua Rd 1688, Hefei 230601, China; c200602003@ahu.edu.cn

<sup>4</sup> Department of Materials Science and Engineering, University of Ioannina, GR-451 10 Ioannina, Greece; sagat@cc.uoi.gr

\* Correspondence: xuxin@ustc.edu.cn

Received: 3 April 2018; Accepted: 1 May 2018; Published: 2 May 2018



**Abstract:** The photocatalytic activity in the range of visible light wavelengths and the thermal stability of the structure were significantly enhanced in Si, N co-doped nano-sized TiO<sub>2</sub>, and synthesized through high-energy mechanical milling of TiO<sub>2</sub> and SiO<sub>2</sub> powders, which was followed by calcination at 600 °C in an ammonia atmosphere. High-energy mechanical milling had a pronounced effect on the mixing and the reaction between the starting powders and greatly favored the transformation of the resultant powder mixture into an amorphous phase that contained a large number of evenly-dispersed nanocrystalline TiO<sub>2</sub> particles as anatase seeds. The experimental results suggest that the elements were homogeneously dispersed at an atomic level in this amorphous phase. After calcination, most of the amorphous phase was crystallized, which resulted in a unique nano-sized crystalline-core/disordered-shell morphology. This novel experimental process is simple, template-free, and provides features of high reproducibility in large-scale industrial production.

**Keywords:** Si, N co-doped anatase; high-energy mechanical milling; mechanochemical method; photocatalytic activity

## 1. Introduction

The strong and increasing presence of organic contaminants currently in the environment leads to many studies about photocatalytic degradation of photocatalytic materials. Titanium dioxide (TiO<sub>2</sub>) is a very popular material in such applications and it owes its existence to its non-toxicity, high chemical stability, low cost, and good optoelectronic properties [1–5]. Anatase, which is one of the mineral forms of TiO<sub>2</sub>, is more active under ultraviolet (UV) light irradiation than the other TiO<sub>2</sub> crystalline phases such as brookite and rutile [6–8]. Anatase TiO<sub>2</sub> has a 3.2 eV wide band gap. Nevertheless, due to this value, only an approximate 3% of the arriving solar energy on earth can be used by anatase TiO<sub>2</sub> [9–11].

Anatase TiO<sub>2</sub> is thermodynamically a high-temperature metastable structure, which can irreversibly transform into rutile TiO<sub>2</sub> after calcination at ca. 600 °C. Although rutile has a smaller band gap (=3.0 eV) than anatase, it exhibits poor photocatalytic activity because of the intrinsic features

of the crystalline structure of rutile [12–14]. Furthermore, anatase TiO<sub>2</sub> synthesized at low temperatures has poor crystallinity, which deteriorates its photocatalytic activity [15].

For the sake of substantially improving the solar energy as well as the thermal stability of anatase TiO<sub>2</sub>, many studies have reported on the development of photocatalysts, which display high activity by irradiation with ultraviolet light as well as in the range of visible light [16–19]. The visible-light response of N-doped TiO<sub>2</sub> was covered initially in 1986 by Sato [20]. Since then, many research groups have reported on the visible-light response of N-doped TiO<sub>2</sub> materials produced by various approaches. Nonetheless, N is not stable in TiO<sub>2</sub> at high temperatures since it can be decomposed at about 600 °C [21]. In our earlier study, anatase TiO<sub>2</sub> was also doped with Si, which resulted in a stable anatase phase at high calcination temperatures. The high thermal stability of N in anatase TiO<sub>2</sub> was attributed to the existence of Si-N bonds in TiO<sub>2</sub> [22]. It was also demonstrated that the homogeneous dispersion of Si in the TiO<sub>2</sub> crystal plays an important role in photocatalytic activity.

High-energy mechanical milling is often utilized to synthesize various non-equilibrium and equilibrium alloy or ceramic phases [23–25]. This solid-state powder processing includes repeated fracture, welding, and re-welding of powder particles. Therefore, it can produce highly homogeneous precursors and equally homogeneous resultant powders. Currently, high-energy mechanical milling is also considered an effective process for synthesizing a variety of non-equilibrium nano-structured phases [26,27].

This paper proposes the high-energy ball-mill solid-state reaction method for synthesizing Si, N co-doped nano-sized anatase TiO<sub>2</sub> because it is a simple and template-free process. It ensures high reproducibility and exhibits a great potential for large-scale industrial production.

## 2. Materials and Methods

Fine powders of anatase TiO<sub>2</sub>, rutile TiO<sub>2</sub> and nano-SiO<sub>2</sub> were used as raw materials (Aladdin Chemical Co., Ltd., Shanghai, China). First, powders of TiO<sub>2</sub> doped with Si were prepared. These samples had various weight ratios of Ti/Si, which were 0.999:0.001, 0.995:0.005, 0.99:0.01, 0.98:0.02, and 0.96:0.04. Hereafter, these samples are simply denoted as 0.1Si, 0.5Si, 1Si, 2Si, and 4Si, respectively. The mixtures of TiO<sub>2</sub> and SiO<sub>2</sub> powders were ground in an agate mortar by hand for 20 min. This manually-prepared mixture was transferred to a silicon nitride ball-milling tank of a high-energy ball mill. The milling speed was set as 800 rpm and the milling time as 6 h.

A non-doped (i.e., with no Si) sample of pure anatase TiO<sub>2</sub>, denoted as 0Si, was also prepared under the same conditions of high-energy ball milling.

In order to investigate the influence of the speed of ball-milling, the sample 2Si was subjected to ball-milling at various speeds. More specifically 500 rpm, 600 rpm, and 800 rpm and these samples are denoted as H-500, H-600, and H-800, respectively.

To produce the Si, N co-doped TiO<sub>2</sub> samples, the obtained Si-doped TiO<sub>2</sub> powders (0Si–4Si) were transferred to Al<sub>2</sub>O<sub>3</sub> crucibles and then calcined at 600 °C for 4 h in an atmosphere of a flowing gas mixture of ammonia (50%)/N<sub>2</sub> (50%) in a high-temperature tubular electric furnace. The heating rate was set as 4 K/min. After the thermal treatment, the samples were cooled down to room temperature naturally. These Si, N co-doped samples are designated as 0Si-N, 0.1Si-N, 0.5Si-N, 1Si-N, 2Si-N, and 4Si-N.

Two samples with a Ti/Si ratio of 0.98:0.02 were produced similarly using rutile TiO<sub>2</sub> and they are denoted as R-2Si, R-2SiN.

The identification of the crystalline phases was carried out by XRD (X-ray diffraction analysis, PW 1700, Philips Research Laboratories, Eindhoven, The Netherlands) using Cu K<sub>α1</sub> radiation and  $\alpha$  scanning rate of 2 °C/min. The nano-structure of the samples was observed using an HRTEM (high-resolution transmission electron microscope, JEOL-2010, JEOL, Tokyo, Japan). An EDS (energy dispersive X-ray spectrometer), FTIR (Fourier transform infrared spectra, Nicolet 8700, Thermo Scientific, Waltham, MA, USA), and XPS (X-ray photoelectron spectra, ESCALAB 250, Thermo-VG Scientific, USA) were used for elemental and chemical bond analysis. Thermal analysis of the samples

was conducted (DTA-TGA, DTG-60H, Shimadzu, Kyoto, Japan) at a heating rate of 10 K/min up to 1200 °C. The specific pore volume and surface area were determined with Barrett-Joyner-Halenda (BJH) and Brunauer-Emmett-Teller (BET) reanalysis by using Micromeritics Tristar II 3020M equipment (Micromeritics, Norcross, GA, USA). The photoluminescence properties of the produced samples were measured by using the fluorescent spectrophotometer (PL, F-4600, Hitachi Ltd., Tokyo, Japan) with a 200 W Xe-lamp as an excitation source at room temperature. The UV-visible spectrophotometer (SOLID 3700, Shimadzu Ltd., Kyoto, Japan) was used to measure UV-visible diffuse reflectance spectra of the produced samples.

The photocatalytic activity was surveyed by the decomposition of RhB (Rhodamine B). In a representative experiment, the 50 mg synthesized catalyst powder were added to a 50 mL RhB aqueous solution with a concentration of 10 mg/L in a clean quartz reactor. The suspension liquid was magnetically stirred with uniform speed in a dark room for 30 min before using illumination to establish adsorption/desorption equilibrium between the surface of the photocatalyst and RhB. After that, an Xe lamp of 500 W was used as a UV-visible light source. The 5 mL mixture was centrifuged with 8000 rpm rotational speed to remove the catalyst particles and take them out in fixed illumination time intervals. The RhB concentration was determined by a UV-visible spectrophotometer (UV-759, Shanghai Precision & Scientific Instrument Co., Ltd., Shanghai, China). For comparison, the photocatalytic activity of a commercial photo catalyst Degussa P25 TiO<sub>2</sub> (Evonik Degussa, Essen, Germany), raw anatase, and raw rutile were also measured under the same condition.

### 3. Results and Discussion

#### 3.1. Crystalline Structure, Nanostructure, and Elemental Analysis

The diffractograms in Figure 1 suggest that the speed of ball-milling has a significant impact on the crystalline structure of the (non-calcined) produced samples. More specifically, the diffraction peaks of the anatase phase become markedly weaker and broader when the speed of the high-energy ball-milling increases. This is clearly observed in the peak of the plane (101) at ~25.3°. The reduction in the intensity of the peaks suggests that the highly crystallized anatase phase gradually shifts to a regime of an amorphous state along with a considerable refinement in the size of the particles. The average dimension of the crystallites (*D*), calculated by the Scherrer equation [28,29],  $D = K\lambda/B\cos\theta$ , where *K* is a constant near 1,  $\lambda$  is the wavelength of the X-ray radiation, *B* is the FWHM (full width at half maximum), and  $\theta$  is the angle of diffraction, were 73.54 nm, 42.12 nm, 27.39 nm, and 17.01 nm for the samples of TiO<sub>2</sub> raw anatase, H500, H600, and H800, respectively.

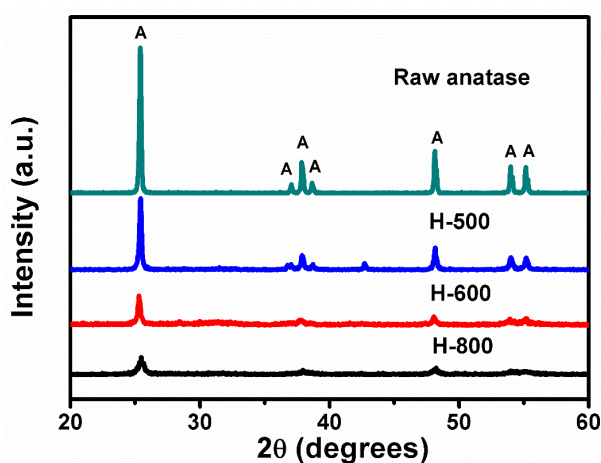
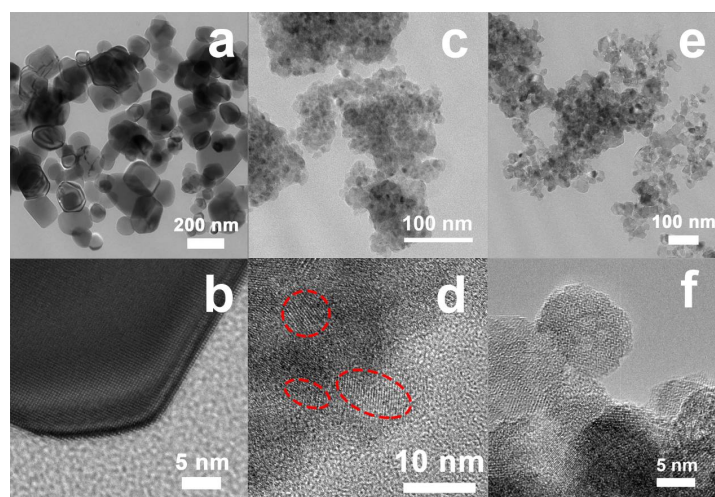


Figure 1. Influence of ball-milling speed on the crystalline structure (A: anatase TiO<sub>2</sub>, JCPDS#21-1272).

These results are in broad agreement with the images of TEM and HRTEM (see Figure 2a–d). The powder of raw anatase TiO<sub>2</sub> is well crystallized and the particle size ranges between 50 nm and 200 nm (see Figure 2a,b). High-energy ball-milling at 800 rpm resulted in a significant decrease in particle size in the sample 2Si down to about 5~10 nm, which was observed in the areas included inside the dashed lines in Figure 2d and features of amorphous material are also observed (see Figure 2c,d).



**Figure 2.** Transmission electron microscope (TEM) (a,c,e) and high-resolution transmission electron microscope (HRTEM) (b,d,f) images of the powders of the raw anatase TiO<sub>2</sub> (a,b) and the samples 2Si (c,d) and 2Si-N (e,f) milled at the speed of 800 rpm.

The above results suggest that the mechano-chemical processing via the high-energy ball-milling causes violent collision, grinding, and an abrasive effect on the powder, which resulted in grain refinement and eventually destroyed the original surface of the powder as far as its morphology and chemistry are concerned. Therefore, the surface lattice of the TiO<sub>2</sub> crystal is transformed to an amorphous layer and the crystalline regime decays.

The diffractograms in Figure 3, which were obtained from the Si-free sample (0Si-N) and Si, N co-doped samples 0.1Si-N–4Si-N calcined at 600 °C and demonstrate the essential role of Si in the formation of anatase phase in the final product. More specifically, the rutile phase was solely formed in the sample 0Si-N while pure anatase was developed in the 2Si-N and 4Si-N powders. Anatase was predominantly formed in the samples 0.1Si-N–1Si-N, but small peaks attributed to traces of the rutile phase were also recorded in these samples.

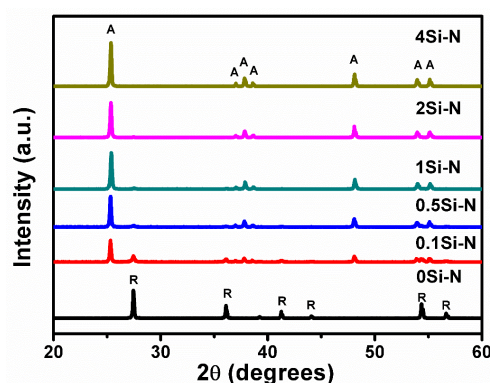


**Figure 3.** Influence of Si-content on the crystalline structure of the Si, N co-doped samples and the Si-free sample 0Si-N (A: anatase TiO<sub>2</sub>, JCPDS#21-1272, R: rutile TiO<sub>2</sub>, JCPDS#21-1276).

Nonetheless, the X-ray diffractograms of Figure 4 suggest that the presence of anatase seeds is necessary in order to get anatase. To be more specific, these diffractograms show that in the rutile-containing samples R-2Si and R-2SiN, rutile is exclusively formed regardless of the fact that they both contained Si. However, high-energy ball-milling also caused reduction in the crystallinity in these samples, which was suggested by the widening of the diffraction peaks while calcination improved crystallinity (i.e., the peaks become sharper from R-2Si to R-2SiN with the latter being calcined at 600 °C).

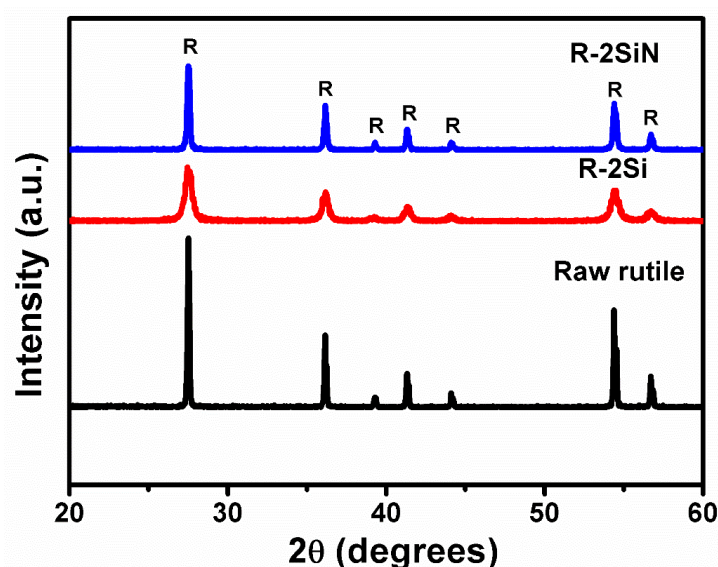


Figure 4. X-ray diffractograms of the rutile-containing samples.

The TEM and HRTEM images of the sample 2Si-N, shown in Figure 2e,f, respectively, suggest that this powder (2Si-N) is uniform (i.e., it exhibits a narrow particle size distribution) with a particle size of about 40 nm to 50 nm. Accordingly, mechanical milling should favor diffusion and atomic rearrangements of the starting powders. The homogeneous amorphous mixture should eventually lead to formation of anatase phase where Si should be uniformly distributed. As a result, a unique nano-sized crystalline-core/disordered-shell morphology is observed.

The sample 2Si-N was thoroughly analyzed by EDS, FTIR, and XPS (see Figure 5). The presence of TiO<sub>2</sub> is indicated by the peaks at 0.5 keV for O and 4.5 keV and 4.9 keV for Ti (EDS, Figure 5a). The presence of N and Si is confirmed by the peaks of N (0.4 keV) and Si (1.7 keV). Nitrogen contents determined by the XPS were 0.09%, 0.15%, 2.15%, 3.21%, and 4.33% for the sample nSi-N (n = 0.1, 0.5, 1, 2, and 4), respectively.

In the FTIR spectra of raw anatase and the samples 2Si and 2Si-N (see Figure 5b), a broad band at 2700–3600 cm<sup>-1</sup> attributed to O-H stretching vibrations of water, a peak at 1635 cm<sup>-1</sup> was ascribed to the flexion vibrations of the O-H groups [30,31]. A broad band at 400–800 cm<sup>-1</sup>, which is owed to the stretching vibrations of O-Ti-O and Ti-O bonds [32,33], was recorded. In the sample 2Si-N, the absorption peak of Si-N bond, situated at 890 cm<sup>-1</sup>, was also observed [34].

The presence of Si-N and Si-O bonds was also confirmed by the XPS analysis. More specifically, the two peaks at 102.7 eV and 101.7 eV correspond to the Si-N and Si-O bonds, respectively (see Figure 5c) [35,36]. Three peaks are discovered in the spectrum of N 1s (see Figure 5d). The peaks at 399.9 eV and 401.8 eV are ascribed to Ti-O-N or Ti-N-O, respectively [37–39]. The peak at 396.5 eV is due to negatively-charged nitrogen that substitutes oxygen and forms Si-N and Ti-N bonds in the lattice of TiO<sub>2</sub> [39]. An O 1s core level peak emerges at ca. 529.5 eV, 530.9 eV, and 532.1 eV (see Figure 5e) [35,36,40]. The peak at 529.5 eV is the main peak, which can be ascribed to the oxygen

in Ti-O-Ti. The peak at 530.9 eV is attributed to Ti-O-Si linkage and the peak at 532.1 eV is attributed to the O-H band on account of the water adsorption.

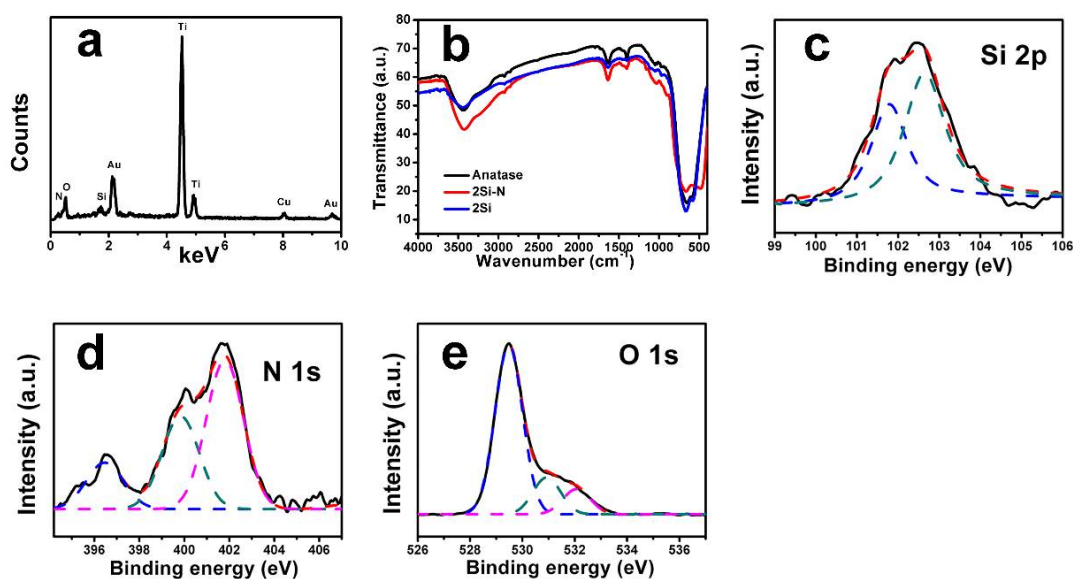


**Figure 5.** Results of (a) energy dispersive X-ray spectrometer (EDS) (the peaks at 2.1 keV and 9.7 keV are due to the conductive Au coating), (b) Fourier transform infrared spectra (FTIR), and (c,d,e) X-ray photoelectron spectra (XPS) analyses of the sample 2Si-N.

The thermal analysis of the sample 2Si-N (see Figure 6) showed a slight weight loss below 600 °C. This occurred because of the evaporation of the adsorbed, crystallized water as well as the decomposition of the ammonium groups in the sample. The two weak endothermic peaks close to 800 °C and a small weight loss in the range 800 °C to 1000 °C might be attributed to the decomposition/release of internal N. The weight loss at temperatures higher than 1000 °C might be ascribed to a result coming from the breaking of Si-N bonds. The results are in satisfactory agreement with our previous reports [22], which confirms the stability of the obtained sample.

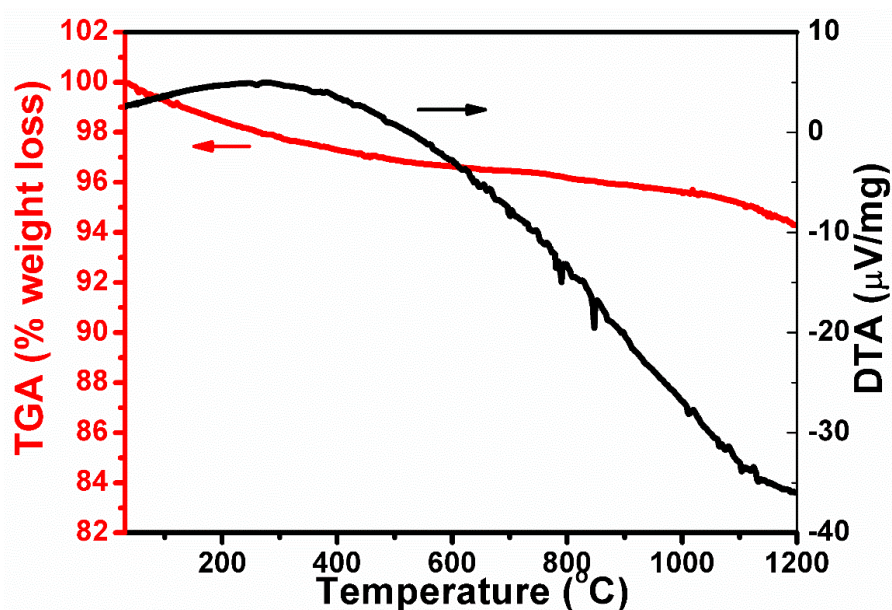


**Figure 6.** Results of thermal analysis (DTA and TGA) of the sample 2Si-N.

### 3.2. Textural Parameters

In this section, the key features, which are closely related to the catalytic efficiency of the produced photocatalysts are presented using namely texture, photoluminescence properties (emission spectra and UV-visible diffuse spectra), and photocatalytic activity, which were experimentally determined by the degradation of RhB.

Texture, associated with specific surface area and pore size distribution, is an important feature of a catalyst. The  $N_2$  adsorption-desorption curves of the samples 2Si-N and raw anatase  $TiO_2$  powder were experimentally recorded and the results are plotted in Figure 7. It is immediately concluded that the raw anatase  $TiO_2$  powder is a well-crystallized and a non-porous material because of the absence of the hysteresis loop. On the contrary, the hysteresis loop between the adsorption and desorption isotherms in the sample 2Si-N suggests that a microporous structure was developed as a result of the high-energy ball-milling treatment, which led to an increase in the specific surface area from  $45.40 \text{ m}^2/\text{g}$  for the raw  $TiO_2$  to  $107.69 \text{ m}^2/\text{g}$  in the sample 2Si-N.

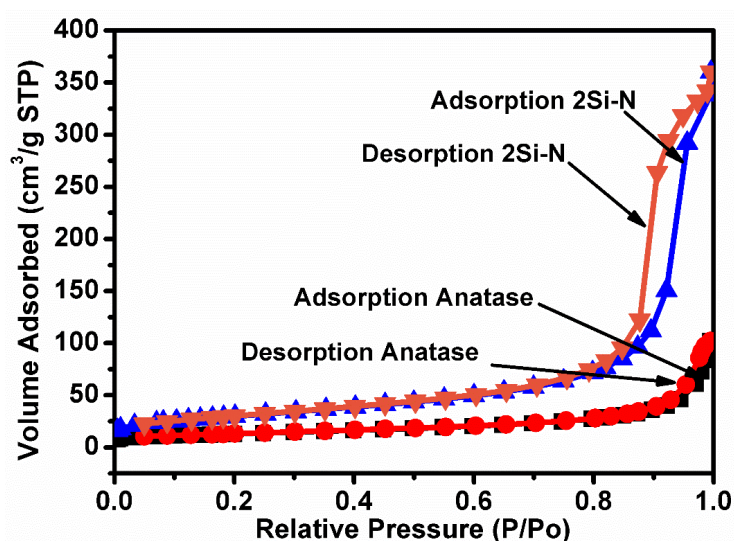


Figure 7.  $N_2$  adsorption/desorption isotherms of the samples 2Si-N and raw anatase  $TiO_2$  powder.

### 3.3. Optical Properties

The optical properties of the solid material are often correlated to the microstructure with regard to its influence on the electron state, the defect state, and energy levels [41,42]. In the particular case of nano-structured materials, the photoluminescence spectra are closely related to the migration of photo-generated electrons and holes as well as their separation and recombination rate.

The photoluminescence properties of the produced samples are reported in the emission spectra of Figure 8. The emission spectrum of raw anatase powder was also recorded for comparison purposes. Two peaks were recorded at 410 nm and 470 nm. The former (410 nm) should correspond to the forbidden band width of the anatase phase  $TiO_2$  [43]. The latter (470 nm) should be mainly due to oxygen vacancies or defects on the surface of  $TiO_2$ . The highest emission intensity was recorded in the raw anatase powder. Additionally, a small amount of Si (0.1Si-N) immediately caused a decrease in the intensity. The lowest intensity was recorded in the sample 2Si-N.

These results suggest that Si doping should cause a certain defect to the  $TiO_2$  lattice, which acts as an electron-capturing agent. The theory suggests that the utilization of photo-generated electrons and holes increases when the photo-generated electrons and holes are effectively separated. Accordingly, the decrease in fluorescence intensity from the 0.1Si-N sample to the 2Si-N sample should mean that the photo-generated electron-hole separation is suppressed with the increase in Si content (in this range of Si-content). Nonetheless, a further increase in the Si led to an increase in fluorescence intensity.

This might be attributed to formation of many defects in the  $\text{TiO}_2$  lattice, which should act as a recombination center of the photo-generated electron-hole composite. This enhances the fluorescence in 4Si-N.

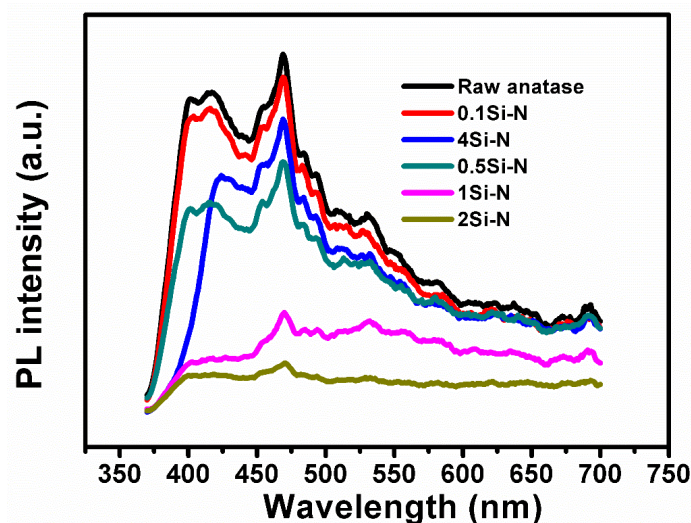


**Figure 8.** Photoluminescence properties (emission spectra) of the produced samples and comparison with raw anatase  $\text{TiO}_2$  powder.

The UV-visible diffuse reflectance spectrum shows the range of the light response of a material. A good photocatalyst must maximize the utilization of the natural light, which means that it must have a large range of light response (shown in the absorption edge, which is the wavelength threshold of light response) and the absorption intensity of the spectrum. The UV-visible diffuse reflectance spectra of the produced samples and the raw anatase and rutile powders are presented in Figure 9.

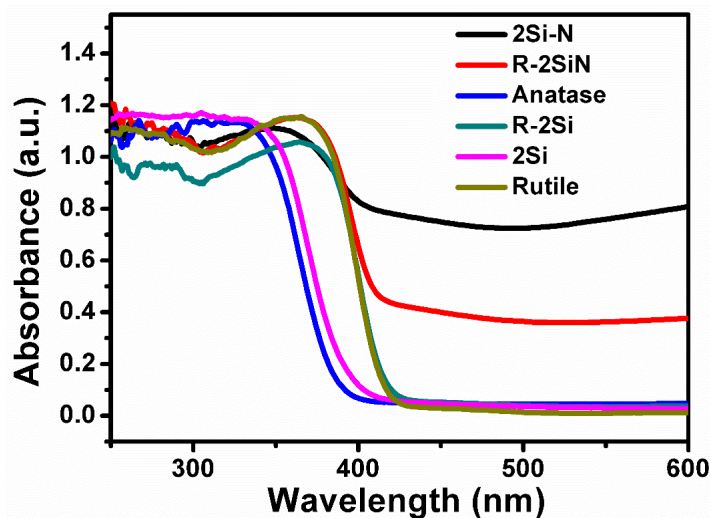


**Figure 9.** UV-visible diffuse reflectance spectra of the produced samples and comparison with raw anatase and rutile powders.

First of all, the absorption edge of the pure rutile  $\text{TiO}_2$  is red-shifted when compared to pure anatase  $\text{TiO}_2$  because of the smaller band gap of anatase  $\text{TiO}_2$  (the band gap of rutile  $\text{TiO}_2$  and anatase  $\text{TiO}_2$  are 3.0 eV and 3.2 eV, separately). However, due to the intrinsic structural features of rutile  $\text{TiO}_2$ , the photocatalytic performance of rutile  $\text{TiO}_2$  is worse than anatase. Single doping of rutile  $\text{TiO}_2$  with



Si via the high-energy ball-milling (which should favor the formation of defects in the sample R-2Si) has a negligible effect on the diffuse reflectance spectra when compared to pure rutile TiO<sub>2</sub>. Co-doping with Si and N in the rutile containing sample R-2SiN only influenced the intensity of absorption in the range of visible light. Accordingly, these results suggest that Si, N co-doping is not expected to improve the photocatalytic properties of rutile TiO<sub>2</sub>.

In the anatase-containing materials, the absorption spectrum of the sample 2Si showed a slight red shift with respect to pure anatase TiO<sub>2</sub>. This can be ascribed to the effect of high-energy ball-milling, which should change the original surface of the TiO<sub>2</sub> crystal, and to the incorporation of Si atoms into the surface. However, a pronounced red shift of the absorption spectrum was achieved in the Si, N co-doped sample 2Si-N. This is clear evidence of the effective and successful doping of N atoms into the TiO<sub>2</sub> lattice of anatase phase, which replaced the O atoms. Accordingly, the energy band of anatase TiO<sub>2</sub> can be suitably adjusted and a larger range of visible light response can be achieved.

### 3.4. Photocatalytic Properties

The plots of Figure 10 actually represent the RhB degradation in an aqueous solution over exposure time in a UV-visible light irradiation by an Xe lamp of 500 W, which is a direct index of the photocatalytic activity of the produced materials in comparison with raw powders of P25, anatase, and rutile TiO<sub>2</sub>. As indicated in the experimental part, the suspension with the photocatalyst was placed in a dark room for 30 min, which established adsorption/desorption equilibrium between the surface of the photocatalyst and RhB and then turned on the illuminant. Therefore, the decline of RhB concentration in this stage between −30 min and 0 min reflects the RhB adsorption behavior. During this step, the results show that the adsorption behavior of RhB on the samples 0Si-N, R-2SiN, and the raw rutile TiO<sub>2</sub> were very weak. This means that the TiO<sub>2</sub> rutile phase has low adsorption ability for RhB. On the contrary, the adsorption ability of the anatase-containing samples raw anatase and 0.1Si-N–4Si-N were certainly higher than the rutile phase and it increased with the rise in the content of Si in the anatase phase. In the low Si-content samples 0.1Si-N–1Si-N, which also have small amounts of rutile phase TiO<sub>2</sub> (see Figure 3), the adsorption ability increased with the rise in the content of anatase phase TiO<sub>2</sub>. The samples 2Si-N and 4Si-N had the higher (i.e., the best) adsorption ability.

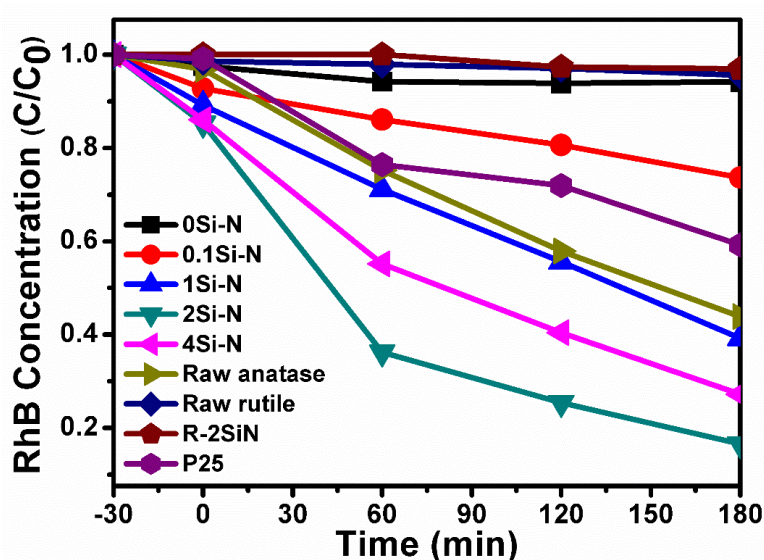


**Figure 10.** Photocatalytic degradation of RhB using the produced samples and raw anatase and rutile powders.

Poor photocatalytic activity of the rutile-containing samples 0Si-N, R-2SiN and the raw rutile TiO<sub>2</sub> was recorded (there is negligible decrease in RhB concentration) while all the anatase-containing

samples displayed much better photocatalytic activity over the investigated exposure time. The moderate photocatalytic activity of the sample 0.1Si-N is ascribed to the co-existence of the rutile phase along with the anatase TiO<sub>2</sub> phase. The photocatalytic property of 1Si-N is better than the raw anatase and P25 because of the co-doped Si and N. The increase in the Si content greatly improved the photocatalytic activity and the best photocatalytic performance was achieved with the sample 2Si-N. Assuming that the increase in Si favors the increase of N incorporation, these results suggest that N incorporation strongly affects the photocatalytic activity of anatase containing powders. N doped TiO<sub>2</sub> photocatalyst makes a smaller band gap and a wider photo response range than the pure TiO<sub>2</sub>. The photo-generated holes on the surface of the photocatalyst abstracts the electrons of the water molecules in the solution, which can generate many highly oxidizing radicals like hydroxyl radicals ( $\bullet\text{OH}$ ), peroxy radical ( $\text{O}^{2-}\bullet$ ), and hydrogen peroxide radicals ( $\bullet\text{HO}^{2-}$ ). The highly oxidizing radicals can decompose the organics and finally convert them into water and carbon dioxide.

Nevertheless, the photocatalytic activity decreases slightly in the sample 4Si-N, which is due to an excess of lattice defects. This means that when Si content is too high, many defects are formed in the TiO<sub>2</sub> lattice, which would act as a recombination center of the photo-generated electron-hole composite and lead to a decrease in the utilization of photo-generated carrier and eventually to a reduction in the photocatalytic activity of the product.

In general, the increase in the photocatalytic activity of the produced Si, N co-doped nano-sized anatase-containing samples can be attributed to the unique crystalline-core/disordered-shell morphology. The synergistic effect owing to the presence of oxygen vacancy's in the bulk anatase crystalline phase and on the surface, which has nearly stoichiometric disorder features, can effectively narrow the band-gap [44].

#### 4. Conclusions

High thermal stability and high photocatalytic activity of Si, N co-doped anatase TiO<sub>2</sub> phase was achieved by high-energy ball-milling and heat treatment of the produced samples in an ammonia atmosphere. The experimental results showed that rutile TiO<sub>2</sub>, co-doped with Si and N evenly, has a poor photocatalytic activity. On the other hand, doping of anatase TiO<sub>2</sub> with 2% Si resulted in samples with pure anatase crystalline phase that exhibited the best photocatalytic activity. This high photocatalytic activity is attributed to the Si-N incorporation and the development of a crystalline-core/disordered-shell morphology. This innovative process is simple and provides features of high reproducibility and suitability for large-scale industrial production.

**Author Contributions:** Xin Xu and Luyuan Hao conceived and designed the experiments; Peisan Wang performed the experiments and wrote the paper; Chunxia Qi and Pengchao Wen analyzed the data; Simeon Agathopoulos contributed analysis tools.

**Acknowledgments:** This research was supported by the National Natural Science Foundation of China (Grant Nos. U1732115 and 51372238) and the CNPC-CAS strategic cooperation research program (2015A-4812).

**Conflicts of Interest:** The authors declare no conflict of interest.

#### References

1. Pueyo, N.; Miguel, N.; Mosteo, R.; Ovelheiro, J.L.; Ormad, M.P. Synergistic effect of the presence of suspended and dissolved matter on the removal of cyanide from coking wastewater by TiO<sub>2</sub> photocatalysis. *J. Environ. Sci. Health Part A* **2017**, *52*, 182–188. [[CrossRef](#)] [[PubMed](#)]
2. Momeni, M.M.; Nazari, Z. Preparation of TiO<sub>2</sub> and WO<sub>3</sub>-TiO<sub>2</sub> nanotubes decorated with PbO nanoparticles by chemical bath deposition process: A stable and efficient photo catalyst. *Ceram. Int.* **2016**, *42*, 8691–8697. [[CrossRef](#)]
3. Bianchi, C.; Stucchi, M.; Pirola, C.; Lanza, M.; Cerrato, G.; Cappellin, L.; Biasioli, F.; Capucci, V. TiO<sub>2</sub> photocatalysis for the abatement of ubiquitous indoor pollutants: Study of the simultaneous degradation of aldehydes. *Trends Photochem. Photobiol.* **2016**, *17*, 31–43.

4. Ahmad, M.; Yingying, S.; Nisar, A.; Sun, H.; Shen, W.; Wei, M.; Zhu, J. Synthesis of hierarchical flower-like ZnO nanostructures and their functionalization by Au nanoparticles for improved photocatalytic and high performance Li-ion battery anodes. *J. Mater. Chem.* **2011**, *21*, 7723–7729. [[CrossRef](#)]
5. Manshor, H.; Aris, S.M.; Azhar, A.Z.A.; Abdullah, E.C.; Ahmad, Z.A. Effects of TiO<sub>2</sub> addition on the phase, mechanical properties, and microstructure of zirconia-toughened alumina ceramic composite. *Ceram. Int.* **2015**, *41*, 3961–3967. [[CrossRef](#)]
6. Pillai, S.C.; Periyat, P.; George, R.; McCormack, D.E.; Seery, M.K.; Hayden, H.; Colreavy, J.; Corr, D.; Hinder, S.J. Synthesis of high-temperature stable anatase TiO<sub>2</sub> photocatalyst. *J. Phys. Chem. C* **2007**, *111*, 1605–1611. [[CrossRef](#)]
7. Li, N.; Liu, G.; Zhen, C.; Li, F.; Zhang, L.; Cheng, H.M. Battery performance and photocatalytic activity of mesoporous anatase TiO<sub>2</sub> nanospheres/graphene composites by template-free self-assembly. *Adv. Funct. Mater.* **2011**, *21*, 1717–1722. [[CrossRef](#)]
8. Dambournet, D.; Belharouak, I.; Amine, K. Tailored preparation methods of TiO<sub>2</sub> anatase, rutile, brookite: Mechanism of formation and electrochemical properties. *Chem. Mater.* **2009**, *22*, 1173–1179. [[CrossRef](#)]
9. Maira, A.; Coronado, J.; Augugliaro, V.; Yeung, K.; Conesa, J.; Soria, J. Fourier transform infrared study of the performance of nanostructured TiO<sub>2</sub> particles for the photocatalytic oxidation of gaseous toluene. *J. Catal.* **2001**, *202*, 413–420. [[CrossRef](#)]
10. Lin, Z.; Orlov, A.; Lambert, R.M.; Payne, M.C. New insights into the origin of visible light photocatalytic activity of nitrogen-doped and oxygen-deficient anatase TiO<sub>2</sub>. *J. Phys. Chem. B* **2005**, *109*, 20948–20952. [[CrossRef](#)] [[PubMed](#)]
11. Liang, Y.; Zhou, B.; Li, N.; Liu, L.; Xu, Z.; Li, F.; Li, J.; Mai, W.; Qian, X.; Wu, N. Enhanced dye photocatalysis and recycling abilities of semi-wrapped TiO<sub>2</sub>@ carbon nanofibers formed via foaming agent driving. *Ceram. Int.* **2018**, *44*, 1711–1718. [[CrossRef](#)]
12. Zhou, W.; Sun, F.; Pan, K.; Tian, G.; Jiang, B.; Ren, Z.; Tian, C.; Fu, H. Well-Ordered Large-Pore Mesoporous Anatase TiO<sub>2</sub> with Remarkably High Thermal Stability and Improved Crystallinity: Preparation, Characterization, and Photocatalytic Performance. *Adv. Funct. Mater.* **2011**, *21*, 1922–1930. [[CrossRef](#)]
13. Reidy, D.J.; Holmes, J.D.; Nagle, C.; Morris, M.A. A highly thermally stable anatase phase prepared by doping with zirconia and silica coupled to a mesoporous type synthesis technique. *J. Mater. Chem.* **2005**, *15*, 3494–3500. [[CrossRef](#)]
14. Huang, P.J.; Chang, H.; Yeh, C.T.; Tsai, C.W. Phase transformation of TiO<sub>2</sub> monitored by Thermo-Raman spectroscopy with TGA/DTA. *Thermochim. Acta* **1997**, *297*, 85–92. [[CrossRef](#)]
15. Kawahara, T.; Konishi, Y.; Tada, H.; Tohge, N.; Nishii, J.; Ito, S. A patterned TiO<sub>2</sub> (anatase) /TiO<sub>2</sub> (rutile) bilayer-type photocatalyst: Effect of the anatase/rutile junction on the photocatalytic activity. *Angew. Chem. Int. Ed.* **2002**, *41*, 2811–2813. [[CrossRef](#)]
16. Umebayashi, T.; Yamaki, T.; Tanaka, S.; Asai, K. Visible light-induced degradation of methylene blue on S-doped TiO<sub>2</sub>. *Chem. Lett.* **2003**, *32*, 330–331. [[CrossRef](#)]
17. Ohno, T.; Mitsui, T.; Matsumura, M. Photocatalytic activity of S-doped TiO<sub>2</sub> photocatalyst under visible light. *Chem. Lett.* **2003**, *32*, 364–365. [[CrossRef](#)]
18. Irie, H.; Watanabe, Y.; Hashimoto, K. Carbon-doped anatase TiO<sub>2</sub> powders as a visible-light sensitive photocatalyst. *Chem. Lett.* **2003**, *32*, 772–773. [[CrossRef](#)]
19. Asahi, R.; Morikawa, T.; Ohwaki, T.; Aoki, K.; Taga, Y. Visible-light photocatalysis in nitrogen-doped titanium oxides. *Science* **2001**, *293*, 269–271. [[CrossRef](#)] [[PubMed](#)]
20. Sato, S. Photocatalytic activity of NO<sub>x</sub>-doped TiO<sub>2</sub> in the visible light region. *Chem. Phys. Lett.* **1986**, *123*, 126–128. [[CrossRef](#)]
21. Sato, S.; Nakamura, R.; Abe, S. Visible-light sensitization of TiO<sub>2</sub> photocatalysts by wet-method N doping. *Appl. Catal. A Gen.* **2005**, *284*, 131–137. [[CrossRef](#)]
22. Wen, P.C.; Ji, W.W.; Zhong, H.; Li, L.; Zhang, B.; Hao, L.Y.; Xu, X.; Agathopoulos, S. Synthesis, characterization and photo-catalytic performance of meso-porous Si-N co-doped nano-spherical anatase TiO<sub>2</sub> with high thermal stability. *RSC Adv.* **2016**, *6*, 110741–110749. [[CrossRef](#)]
23. Koch, C.C. Synthesis of Nanostructured Materials by Mechanical Milling: Problems and Opportunities. *Nanostruct. Mater.* **1997**, *9*, 13–22. [[CrossRef](#)]
24. Xu, X.; Nishimura, T.; Hirosaki, N.; Xie, R.J.; Zhu, Y.C.; Yamamoto, Y. New strategies to prepare nano-sized silicon nitride ceramics. *J. Am. Ceram. Soc.* **2005**, *88*, 934–937. [[CrossRef](#)]

25. Xu, X.; Nishimura, T.; Hirotsaki, N.; Xie, R.J.; Yamamoto, Y.; Tanaka, H. Fabrication of  $\beta$ -sialon nano-ceramics by high-energy mechanical milling and spark plasma sintering. *Nanotechnology* **2005**, *16*, 1569–1573. [[CrossRef](#)]
26. Rongeat, C.; Jansa, I.L.; Oswald, S.; Schultz, L.; Gutfleisch, O. Mechanochemical synthesis and XPS analysis of sodium alanate with different additives. *Acta Mater.* **2009**, *57*, 5563–5570. [[CrossRef](#)]
27. Xu, X.; Tang, J.Y.; Nishimura, T.; Hao, L.Y. Synthesis of Ca- $\alpha$ -SiAlON Phosphors by a Mechanochemical Activation Route. *Acta Mater.* **2011**, *59*, 1570–1576. [[CrossRef](#)]
28. Yu, C.; Jimmy, C.Y. A simple way to prepare C–N-codoped TiO<sub>2</sub> photocatalyst with visible-light activity. *Catal. Lett.* **2009**, *129*, 462. [[CrossRef](#)]
29. Yin, H.; Wada, Y.; Kitamura, T.; Kambe, S.; Murasawa, S.; Mori, H.; Sakata, T.; Yanagida, S. Hydrothermal synthesis of nanosized anatase and rutile TiO<sub>2</sub> using amorphous phase TiO<sub>2</sub>. *J. Mater. Chem.* **2001**, *11*, 1694–1703. [[CrossRef](#)]
30. Nakamura, R.; Ueda, K.; Sato, S. In situ observation of the photoenhanced adsorption of water on TiO<sub>2</sub> films by surface-enhanced IR absorption spectroscopy. *Langmuir* **2001**, *17*, 2298–2300. [[CrossRef](#)]
31. Bezrodna, T.; Puchkovska, G.; Shymanovska, V.; Baran, J.; Ratajczak, H. IR-analysis of H-bonded H<sub>2</sub>O on the pure TiO<sub>2</sub> surface. *J. Mol. Struct.* **2004**, *700*, 175–181. [[CrossRef](#)]
32. Zhang, J.-Y.; Boyd, I.W.; O'sullivan, B.; Hurley, P.; Kelly, P.; Senateur, J.-P. Nanocrystalline TiO<sub>2</sub> films studied by optical, XRD and FTIR spectroscopy. *J. Non-Cryst. Solids* **2002**, *303*, 134–138. [[CrossRef](#)]
33. Wen, Y.; Ding, H.; Shan, Y. Preparation and visible light photocatalytic activity of Ag/TiO<sub>2</sub>/graphene nanocomposite. *Nanoscale* **2011**, *3*, 4411–4417. [[CrossRef](#)] [[PubMed](#)]
34. Rebib, F.; Tomasella, E.; Bêche, E.; Cellier, J.; Jacquet, M. FTIR and XPS investigations of a-SiO<sub>x</sub>N<sub>y</sub> thin films structure. *J. Phys. Conf. Ser.* **2008**, *100*, 082034. [[CrossRef](#)]
35. Ozaki, H.; Iwamoto, S.; Inoue, M. Effects of amount of Si addition and annealing treatment on the photocatalytic activities of N- and Si-codoped titanias under visible-light irradiation. *Ind. Eng. Chem. Res.* **2008**, *47*, 2287–2293. [[CrossRef](#)]
36. Hou, Y.D.; Wang, X.C.; Wu, L.; Chen, X.F.; Ding, Z.X.; Wang, X.X.; Fu, X.Z. N-doped SiO<sub>2</sub>/TiO<sub>2</sub> mesoporous nanoparticles with enhanced photocatalytic activity under visible-light irradiation. *Chemosphere* **2008**, *72*, 414–421. [[CrossRef](#)] [[PubMed](#)]
37. Zhang, K.; Wang, X.; Guo, X.; He, T.; Feng, Y. Preparation of highly visible light active Fe–N co-doped mesoporous TiO<sub>2</sub> photocatalyst by fast sol–gel method. *J. Nanopart. Res.* **2014**, *16*, 2246. [[CrossRef](#)]
38. Higashimoto, S.; Hikita, K.; Azuma, M.; Yamamoto, M.; Takahashi, M.; Sakata, Y.; Matsuo, M.; Kobayashi, H. Visible Light-Induced Photocatalysis on Carbon Nitride Deposited Titanium Dioxide: Hydrogen Production from Sacrificial Aqueous Solutions. *Chin. J. Chem.* **2017**, *35*, 165–172. [[CrossRef](#)]
39. Cong, Y.; Zhang, J.; Chen, F.; Anpo, M. Synthesis and characterization of nitrogen-doped TiO<sub>2</sub> nanophotocatalyst with high visible light activity. *J. Phys. Chem. C* **2007**, *111*, 6976–6982. [[CrossRef](#)]
40. Kasinathan, K.; Kennedy, J.; Elayaperumal, M.; Henini, M.; Malik, M. Photodegradation of organic pollutants RhB dye using UV simulated sunlight on ceria based TiO<sub>2</sub> nanomaterials for antibacterial applications. *Sci. Rep.* **2016**, *6*, 38064. [[CrossRef](#)] [[PubMed](#)]
41. Wakefield, G.; Keron, H.; Dobson, P.; Hutchison, J. Structural and optical properties of terbium oxide nanoparticles. *J. Phys. Chem. Solids* **1999**, *60*, 503–508. [[CrossRef](#)]
42. Lide, Z.; Mo, C.-M. Luminescence in nanostructured materials. *Nanostruct. Mater.* **1995**, *6*, 831–834. [[CrossRef](#)]
43. Malliga, P.; Pandiarajan, J.; Prithivikumar, N.; Neyvasagam, K. Influence of film thickness on structural and optical properties of sol–gel spin coated TiO<sub>2</sub> thin film. *J. Appl. Phys.* **2014**, *6*, 22–28. [[CrossRef](#)]
44. Naldoni, A.; Allieta, M.; Santangelo, S.; Marelli, M.; Fabbri, F.; Cappelli, S.; Bianchi, C.L.; Psaro, R.; Dal Santo, V. Effect of Nature and Location of Defects on Bandgap Narrowing in Black TiO<sub>2</sub> Nanoparticles. *J. Am. Chem. Soc.* **2012**, *134*, 7600–7603. [[CrossRef](#)] [[PubMed](#)]

